Friction

Research Article

Ultra-low wear of WC/bronze composite prepared by binder jet printing and infiltration via amorphous–crystalline nanocomposite tribofilm

Xinyi Liu[1,3], Yi Ren[1,2,3], Xibo Shao[1,2,3], Jiangkun Fan[1,3,✉], Jinshan Li[1,3,✉]

Cite this article: Liu XY, Ren Y, Shao XB, et al. *Friction* 2026, **14**(12): 9441271. https://doi.org/10.26599/FRICT.2026.9441271

ABSTRACT: Anti-wear performance is vital for the lifespan of moving components. Herein, ultra-low wear, even negative wear, was obtained for the tungsten carbide/bronze composites prepared by additive manufacturing binder jet printing (BJPWC), especially when in sliding contact with SiC ceramic. Sliding interface observation reveals that the promising tribological performance of SiC/BJPWC is ascribed to the *in situ* formed stable tribofilm which can deliver beneficial friction reduction and anti-wear effects. The friction process between SiC balls and WC/bronze composite under varying loads induces the diffusion of Si atoms toward the sliding interface, where they form negative mixing enthalpy and network chemical bonds with other metals, promoting the amorphization of the tribolayer. An *in situ* formed unique nanocomposite protective layer is generated, in which Cu/WC nanocrystals are uniformly dispersed within a silicate amorphous matrix. This unique structure effectively accommodates friction-induced plastic deformation and resists damage. This work can provide some basic understanding for ultra-low-wear materials and guides the selection of sliding counterparts for future applications of additive manufactured components.

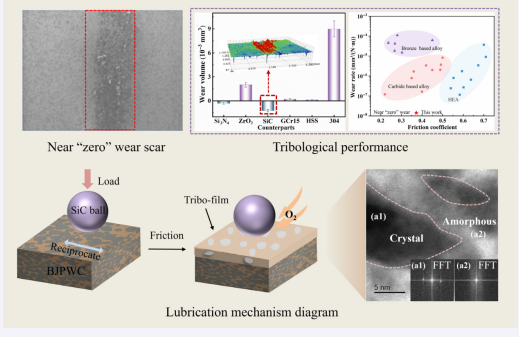

KEYWORDS: additive manufacture; wear; crystal–amorphous; tribofilm

1 Introduction

Additive manufacturing (AM), as an emerging layer-by-layer fabrication strategy, enables unprecedented freedom in shaping complex geometries and engineering tailored microstructures that are unattainable through conventional processing routes. The rapid solidification, localized thermal gradients, and compositional flexibility inherent to AM often lead to refined grains, unique phase distributions, and architectured surfaces, all of which exert a direct influence on friction and wear responses [1–3]. AM is widely employed for multi-material fabrication, functionally graded materials, component repair, and microstructural tailoring to enhance mechanical and tribological performance, while binder jet printing (BJP) provides greater geometric flexibility than conventional manufacturing processes [4, 5]. However, the parts fabricated by the BJP process always exhibit low densification. As a densification process, melt infiltration by some molten alloy through capillary forces is always conducted following the binder jet process [6, 7].

Owing to its binder-mediated consolidation mechanism and broad material compatibility, BJP has been widely applied in the manufacturing of metallic, ceramic, and composite components. Current research primarily focuses on structural metals such as stainless steels [8], nickel-based superalloys [9], and high-entropy alloys [10], where BJP enables the production of near-net-shape parts with tailored porosity and post-sintering densification strategies. In the ceramic field, BJP has been employed to fabricate alumina [11], zirconium carbide [12], tungsten carbide [13], and bio-ceramic scaffolds with controlled interconnected pore architectures for high-temperature, filtration, and biomedical applications. Researchers have carried out some studies into the preparation, structure, and mechanical properties of the parts manufactured through BJP and the alloy infiltration process. For instance, Feng et al. [14] fabricated low-silicon-content SiC ceramics via binder jetting combined with phenolic resin impregnation and pyrolysis (PRIP) and liquid silicon infiltration (LSI), achieving a compressive strength of 7.7±0.3 MPa and low dimensional deviations (1.2–1.6 mm). Cramer et al. [15] fabricated the WC–Co composite through BJP and infiltration, demonstrating that the selection of Co for infiltration can fill the

[1] State Key Laboratory of Solidification Processing, Northwestern Polytechnical University, Xi'an 710021, China. [2] Center of Advanced Lubrication and Seal Materials, Northwestern Polytechnical University, Xi'an 710021, China. [3] School of Materials Science and Engineering, Northwestern Polytechnical University, Xi'an 710072, China.

✉ Corresponding authors. E-mail: J. Fan, jkfan@nwpu.edu.cn; J. Li, ljsh@nwpu.edu.cn

Received: January 7, 2026; Revised: March 30, 2026; Accepted: May 22, 2026

© The Author(s) 2026. This is an open access article under the terms of the Creative Commons Attribution 4.0 International License (CC BY 4.0, http://creativecommons.org/licenses/by/4.0/).

porosity of the WC preforms to form the composite with a near-net-shape composite with minimal shrinkage. Do et al. [16] also suggested that subsequent bronze infiltration can significantly increase the tensile strength of the 420 stainless steel/bronze composite compared with the as-built one.

With the expanding utility of BJP in engineering fields, the tribological performance of materials fabricated via this technique has emerged as a critical area of research. Enrique et al. [17] demonstrated that metal matrix composites can be produced via BJP using Inconel 625 powder and a carbon-containing binder. During sintering, carbon reacts with Cr, Mo, and Nb to form carbides, which evolve into a continuous reinforcing network along particle boundaries. Compared with unreinforced BJP Inconel 625, the resulting composite shows a ~64% reduction in specific wear rate under abrasive conditions [18]. Cui et al. [19] compared the tribological performance of 316SS/bronze (BJP316), 420SS/bronze (BJP420), and WC/bronze (BJPWC) composites against the GCr15 materials, and demonstrated that the wear mechanisms involve abrasion, delamination, and spalling, and that scratch resistance is associated with the soft bronze phase. Wang et al. [20] demonstrated that the BJP 316 stainless steel/bronze composites exhibit a yield strength comparable to that of conventional 316 stainless steel (316SS), while exhibiting markedly enhanced wear resistance in the seawater environment. In the bronze-infiltrated composite, bronze is not only a binder but also a solid lubricant when acting as a moving part. However, the tribological performance of bronze-infiltrated composite towards various parts is still scarce.

In this work, the BJPWC composite with a net-shape structure was fabricated by BJP and subsequent infiltration. To explore its potential application as mechanical components in relative motion, its tribological performance sliding against different counterparts is studied. The results can provide a reference for the potential applications of BJPWC in tribology

2 Experimental

2.1 Material preparation

The spherical WC raw powder (≥ 99.5%) used for BJP is 20–70 μm in size. ExOne's proprietary solvent-based binder was used. The infiltrant material, bronze powder (Sn 11.34%, P 0.32%, Cu Bal., wt%; 45–1,000 μm), was supplied by ExOne. The Innovent printer (ExOne, Innovent, USA) was used to prepare plates with 60 mm in diameter and 13 mm in height. The pre-heating temperature, saturation rate, and layer thickness were 60 °C, 60%, and 100 μm, respectively. Then the job box with the printed plates was placed in an oven for curing at 180 °C for 5 h in an air atmosphere, followed by infiltration of bronze, which was finished inside a vacuum furnace (VBL-57, Solar Manufacturing, USA) at 1,120 °C for 5 h. The hardness of the prepared BJPWC is about 432 HV. The infiltrated plates were subsequently machined into a size of 20 mm × 20 mm × 5 mm for further tests. This process of preparing BJPWC composites is schematically illustrated in Fig. 1(a). The density was measured using a balance (MS204TS/02, Mettler Toledo, Switzerland) based on the Archimedes drainage method. To reduce random errors, three repeated measurements were conducted. The results show that the density of the WC/bronze composite is 13.171±0.0139 g/cm^3.

2.2 Friction tests

The plate surface was ground with SiC waterproof paper to obtain a surface roughness (i.e., R_a) of about 0.1 μm. The friction performance of the BJPWC sliding against different counterparts (SiC, Si_3N_4, ZrO_2, high-speed steel (HSS), GCr15, and 304 stainless steel (304) balls) was evaluated by a ball-on-plate tribometer (UMT TriboLab, Bruker Corporation, USA), with the coefficient of friction (COF) recorded. The test parameters are shown in Table 1. The mechanical properties of these balls are listed in Table 2. The counter-bodies after the friction tests were employed to evaluate the wear rate and wear morphologies using a non-contact three-dimensional (3D) profilometer (Contour GT-K, Bruker Ltd., USA). Specifically, the 3D morphologies and the cross-sectional two-dimensional (2D) profile of the wear-off regions were observed by the 3D profilometer. Every friction test was repeated at least three times to confirm that the results were reproducible.

2.3 Characterizations

The topography of the worn surface against different counterparts was characterized by a scanning electron microscope (SEM; JSM-6490LV, JEOL, Japan) under an accelerating voltage of 15 kV and a working distance of 10 mm. The elemental distribution of the worn surface was observed by an energy-dispersive X-ray spectrometer (EDS; ExOne, Innovent, USA). The volume fraction of the infiltrated bronze in the BJPWC composite was calculated using Image J 1.53a software. The nano-hardness of the alloy surfaces was measured using a nanoindentation instrument (TI980, Hysitron, USA) equipped with a Berkovich diamond tip, with a peak load of 10 mN applied over a loading duration of 5 s. The compressive properties were evaluated using a universal testing machine (3382, Instron, USA) at a strain rate of 10^{-3} s^{-1}. To study the features at the interface and elucidate lubrication and wear mechanisms in play at the tribological contact interface, a lamella from the worn interface of BJPWC rubbed by the SiC ball was prepared by a dual-beam focused ion beam (FIB) system (Helios NanoLab G3 CX, FEI, USA) with a gallium ion source and characterized using an aberration-corrected scanning transmission electron microscope (STEM; ARM 200F, JEOL, Japan). The ion beam system employed a liquid Ga ion source, providing a cross-point resolution better than 2.5 nm at 15 kV. Pt was applied as the protection layer to avoid destruction during milling. During sample preparation, the acceleration voltage was set to 30 kV, with the beam current adjustable from 65 nA to 0.1 pA and a maximum beam current density of up to 65 A/cm^2.

3 Results

The prepared BJPWC composite is observed by SEM. As can be seen in Fig. 1(b), the spherical-like particles with a diameter less than 60 μm are WC, and the rest are bronze. The volume fraction of the infiltrated bronze in the BJPWC composite was estimated to be approximately 43%±4.1%. The SEM images and the corresponding EDS mappings reveal that the contents of C, Cu, Sn, and W are 49.7, 32.0, 2.0, and 16.3 at%, respectively.

To further understand the mechanical response and heterogeneous structure of the WC/bronze composite, nanoindentation tests were performed on the WC and bronze phases, and uniaxial compression tests were conducted on the bulk composite, as shown in Fig. 2. WC exhibits significantly higher indentation resistance than the bronze matrix, indicating its superior stiffness and load-bearing capacity. The hardness of WC (32.81 GPa) is nearly an order of magnitude higher than that of bronze. The elastic modulus of WC (389.41 GPa) is also substantially higher than that of bronze, confirming a strong mechanical contrast between the two phases. The bulk composite shows a nonlinear stress–strain response under compression

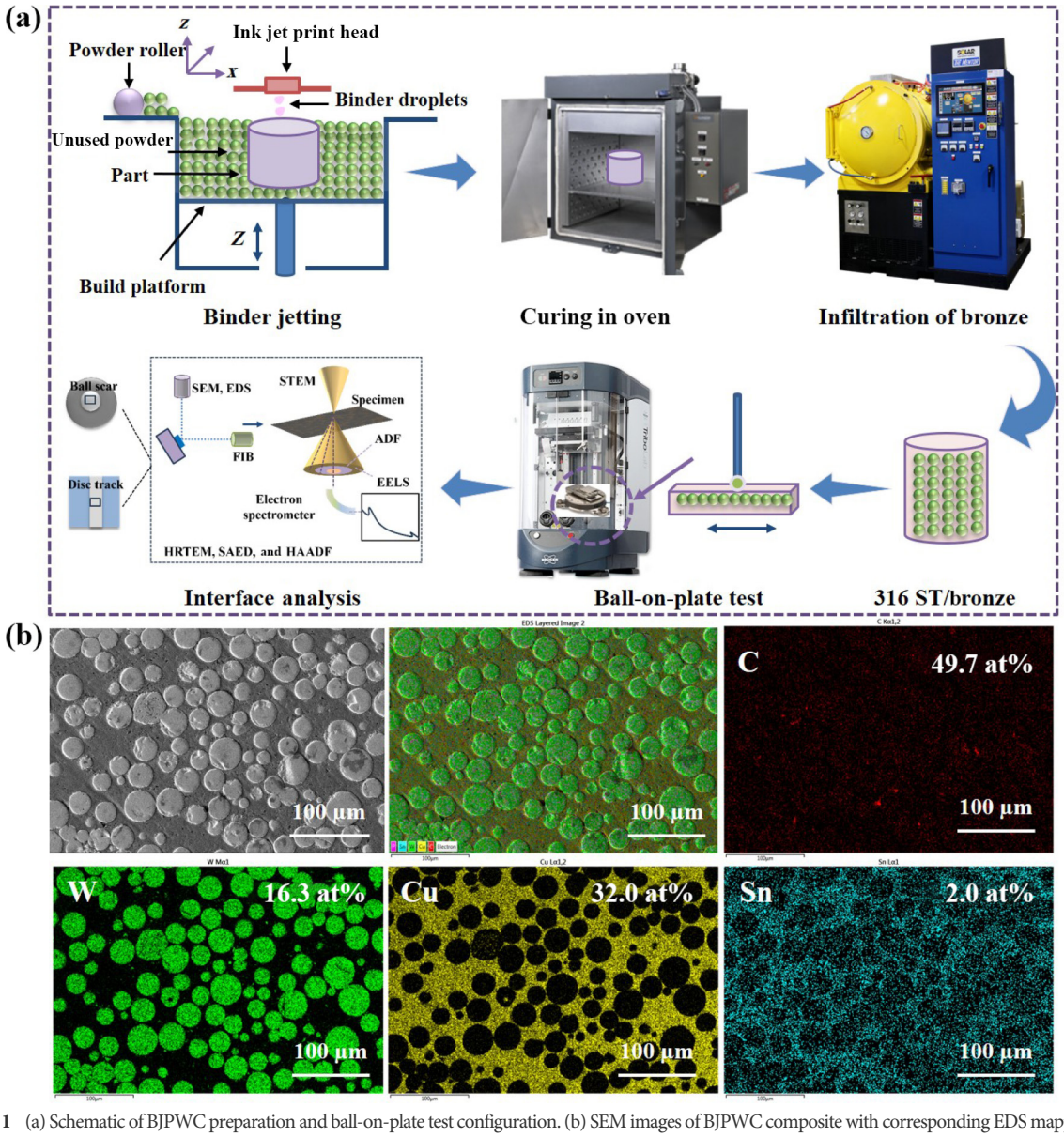

Fig. 1 (a) Schematic of BJPWC preparation and ball-on-plate test configuration. (b) SEM images of BJPWC composite with corresponding EDS mappings.

Table 1 Parameters in friction tests

Plate	BJPWC
Balls	Si_3N_4, ZrO_2, SiC, HSS, GCr15, 304
Applied load	5–80 N
Speed	1–12 Hz
Stroke length	5 mm
Temperature	Room temperature (21–23 °C)
Duration	25 min

Table 2 Mechanical properties of friction counterparts

Balls	Hardness (GPa)	Elastic modulus (GPa)	Poisson's ratio	Thermal conductivity (W/(m·K))
Si_3N_4	14.7	300	0.26	25.0
ZrO_2	11.8	340	0.22	2.0
SiC	27.4	440	0.17	120.0
GCr15	6.9	208	0.30	40.0
HSS	7.2	197	0.30	19.4
304	2.1	193	0.30	16.3

(Fig. 2(c)), with a maximum stress of ~1.2 GPa. No abrupt failure is observed, indicating good structural integrity and effective load transfer between WC and the bronze matrix. Overall, the WC/bronze composite forms a hard–soft heterogeneous structure, where WC provides load-bearing capacity and wear resistance, while the bronze matrix accommodates plastic deformation, contributing to mechanical stability and toughness.

Figure 3 presents the variation of the COF curve with increasing load and sliding frequency when the BJPWC composite slides against different counterpart balls. The repeated tests show similar COF profiles; thus, only instantaneous results from one test are displayed in detail. In addition, the average COF from the repeated tests for different counterpart conditions is presented in Figs. 4(a) and 4(b). The BJPWC composite paired with SiC counterparts exhibits the lowest COF (~0.25) under varying loads. The COF curves for tests with ceramic balls decrease with increasing load (Fig. 3(a)). In contrast, the COF is unstable during sliding against steel balls. In addition, the COF is more sensitive to the applied load for ceramic balls. The friction response for SiC appears to be more positive, with the COF lower than other sliding counterparts (COF < 0.4). Interestingly, SiC

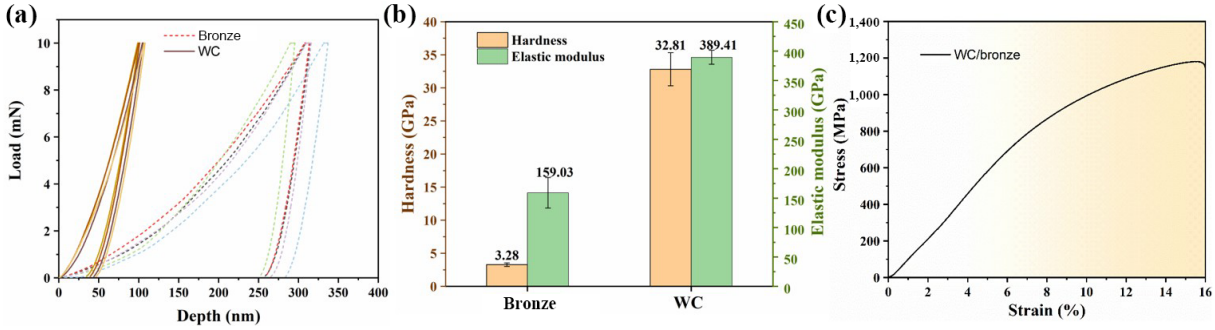

Fig. 2 Mechanical properties of WC/bronze composite. (a) Load–displacement curves under 10 mN load. (b) Hardness and elastic modulus. (c) Compressive stress–strain curves.

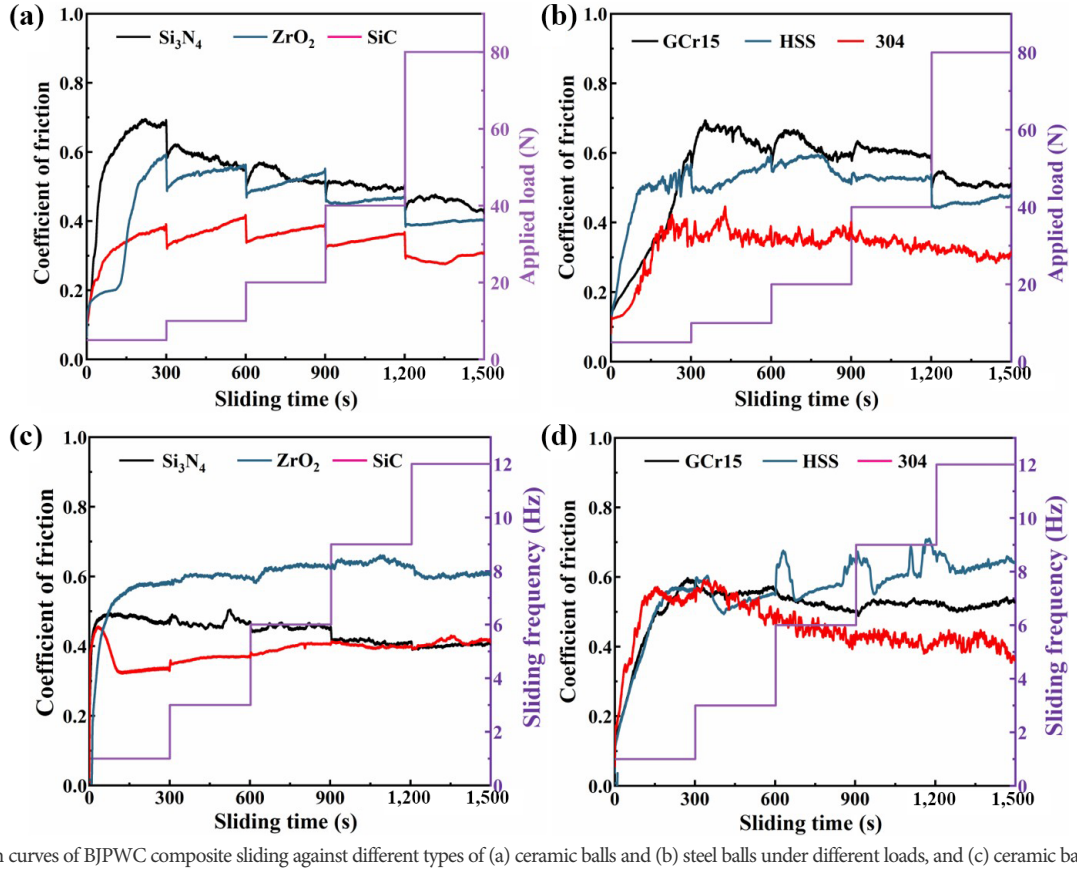

Fig. 3 Friction curves of BJPWC composite sliding against different types of (a) ceramic balls and (b) steel balls under different loads, and (c) ceramic balls and (d) steel balls under different velocities.

exhibits the lowest COF value among the ceramic balls, and the COF of 304 is the lowest in the steel counterparts. The COF data for SiC present the most stable frictional response, with the smallest COF values.

Figure 4(c) shows the wear volume of the WC/bronze composite sliding against different counterpart balls under various conditions. The specimen sliding against 304 steel exhibits the most severe wear, despite its COF being relatively lower than that of other steel counterparts. Sliding with SiC and Si_3N_4 balls under varying loads results in negative wear volumes, indicating the formation of a protective tribofilm on the worn surface due to slight plastic deformation of the bronze matrix and compaction of debris. This phenomenon is not observed under varying sliding frequencies, likely because higher frequencies reduce contact time and remove loosely bonded debris. Among all tested pairs, the WC/bronze composite against SiC consistently exhibits the lowest wear volume, attributed to the high hardness, chemical stability, and weak adhesion of SiC, which promote a stable and protective tribological interface. However, sliding against ZrO_2 results in increased wear. The wear volumes are comparable for HSS and GCr15 under changing load conditions. Figure 4(d) compares the wear performance of the BJPWC composite with other typical tribological materials by plotting wear rate as a function of COF. This result highlights the superior wear resistance and a relatively low COF of the BJPWC composite compared with many conventional materials, demonstrating its strong potential for applications requiring ultra-low wear and high durability.

Similar results can also be inferred from the 3D morphologies and 2D cross-sectional profiles, as shown in Fig. 5. The widths of the wear scar are 0.7, 0.5, 0.6, 0.95, 0.55, and 1.6 mm, respectively, for Si_3N_4, ZrO_2, SiC, GCr15, HSS, and 304. Deep wear tracks are observed on the plates when sliding against ZrO_2 and HSS, while it is minimal for the track of the plate sliding against Si_3N_4 and SiC. The materials above the baseline are the developed tribofilm.

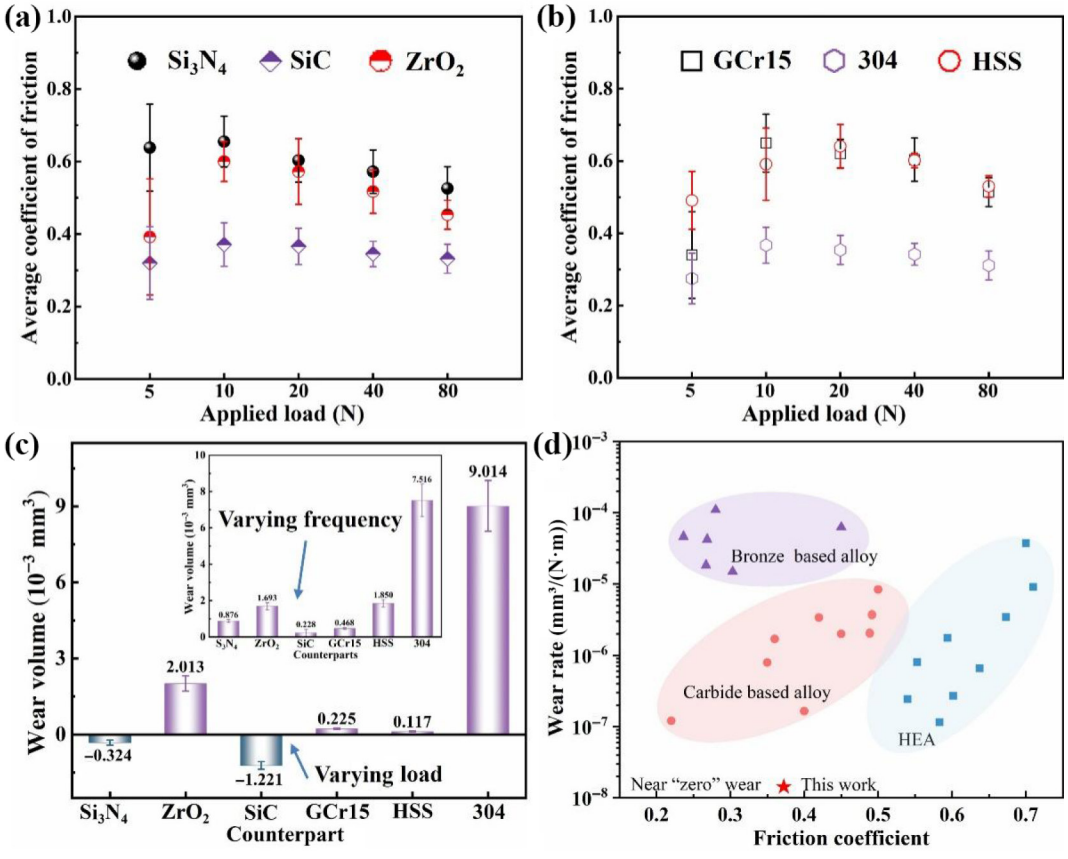

Fig. 4 Average COF and wear volume loss of WC/bronze composite with different counterpart balls: (a) average COF of different ceramic counterpart balls under different loads; (b) average COF of different steel counterpart balls under different loads; (c) total wear volume under various friction test parameters, including sliding for 5 min under different loads (5, 10, 20, 40, and 80 N), with the inset showing sliding for 5 min at different frequencies (1, 3, 6, 9, and 12 Hz); (d) comparison of COF and wear rate of WC/bronze composite with previous work [19–31].

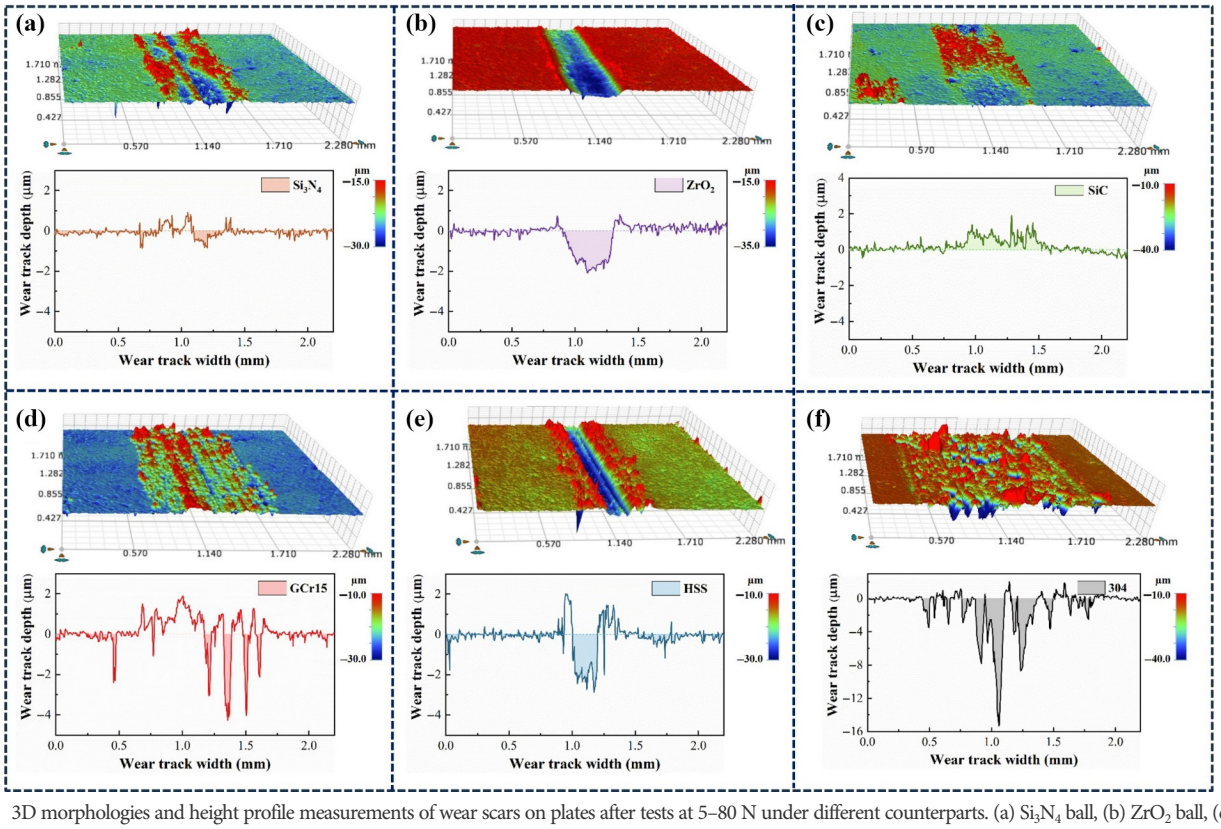

Fig. 5 3D morphologies and height profile measurements of wear scars on plates after tests at 5–80 N under different counterparts. (a) Si_3N_4 ball, (b) ZrO_2 ball, (c) SiC ball, (d) GCr15 ball, (e) HSS ball, and (f) 304 steel ball.

清華大学出版社 Tsinghua University Press | SciOpen

This tribofilm is nearly continuous on the worn surface of SiC, with a thickness of 1–3 μm, which can also be observed in Fig. S3 in the Electronic Supplementary Material (ESM). Almost no measurable wear is involved in the BJPWC/SiC pair. The wear tracks of GCr15 and 304 shown in the 3D profiles are wider than those of other sliding parts.

The secondary electron SEM images and corresponding elemental distributions of the worn surface of the plate are shown in Figs. 6 and 7. For the Si_3N_4-rubbed surface, negligible scratches and peeling off are observed, except for the oxidation in the bronze region. The worn surface still remains smooth. For the ZrO_2-rubbed surface, some debris is identified, where a strong signal of Zr derived from ZrO_2 is observed, suggesting the transfer of the wear debris from the ZrO_2 ceramic ball to the BJPWC plate. When it comes to the worn surface after sliding against SiC, the worn surface is relatively smooth. Interestingly, Cu and O are almost completely covered on the SiC-rubbed worn surface, except for some WC particle regions, which are supposed to be the *in situ* formed tribofilm. The coverage of O and Cu is reduced for the worn surface after tests against Si_3N_4. The coverage of Cu and O is the lowest for ZrO_2. The strength of the signal of O also follows the order that SiC > Si_3N_4 > ZrO_2. The data are consistent with the wear rate results.

In contrast, for the steel-rubbed worn surface, it becomes much rougher than the ceramic-rubbed parts, with a lot of debris, peeling off, and scratches observed on the worn surface, suggesting that abrasive wear is in play during the tests. For the worn surface against the GCr15 ball (Fig. 7(a)), some non-continuous black regions are observed, which are the oxide films, evidenced by the strong O signal in that region. For the HSS-rubbed surface (Fig. 7(b)), the black area is the smeared bronze, identified by the strong Cu signals. For the 304, the worn surface is heavily destroyed, and the WC particles even lose their spherical shape, indicating heavy abrasive wear. The comparable signal of Fe suggests the transfer of steel debris from the ball to the worn surface of the plate (Fig. 7(c)). The presence of numerous irregularly distributed microparticles and the damaged worn surface indicate severe abrasive wear, which also accounts for the noticeable fluctuations in the COF curves.

The degree of wear and morphology of the counterparts also serve as important indicators of the tribological performance of the WC/bronze composite. Figure 8 presents the wear scar morphologies of different counterparts under varying load conditions. For WC/bronze composite/steel balls (Figs. 8(d) and 8(f)), there are obvious deep and dense scratches and grooves parallel to the sliding direction on the surface of 304 steel balls, indicating that the dual ball material has been removed, which is also responsible for the heavy fluctuation of the COF curve in Fig. 3. Differently, the plowing grooves on the surface of HSS and GCr15 steel balls are shallow and less distributed, and significant enrichment of oxygen elements is observed in the corresponding EDS mappings. The dominant wear mechanisms are abrasive wear and oxidative wear. As for the WC/bronze composite with ceramic balls tribo-pair for comparison, smaller patches, ploughs, and oxide particles are observed in Figs. 8(a)–8(c). Similar characteristics of ball material transfer and adhesion are present in the wear scars of Si_3N_4 and ZrO_2 balls. The wear scar of SiC ball is relatively smooth, and no obvious plowing grooves or adhesive wear are observed. EDS mappings show a uniform elemental distribution, with no significant oxidation or material transfer.

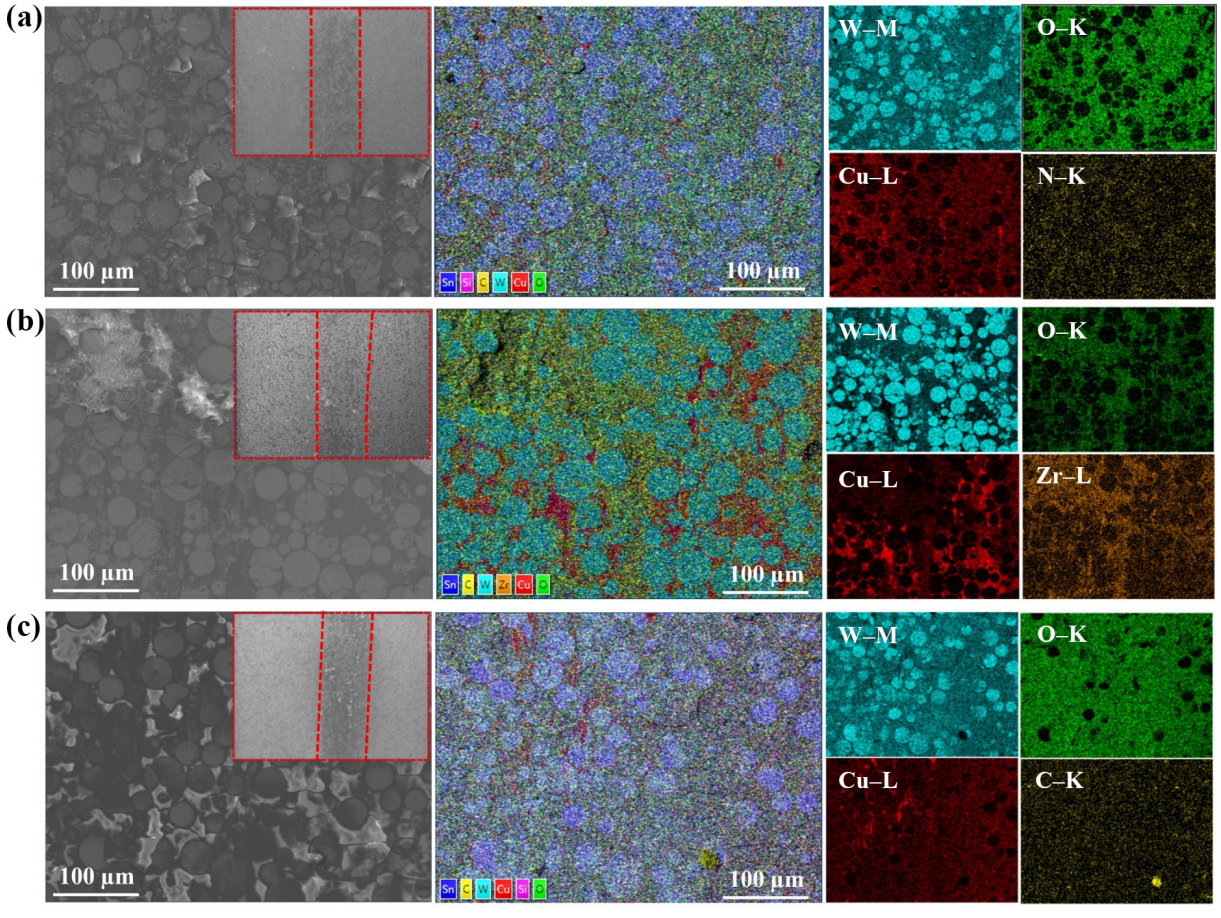

Fig. 6 SEM images and EDS mappings of wear track morphology of BJPWC after tests under different ceramic counterparts: (a) Si_3N_4, (b) ZrO_2, and (c) SiC.

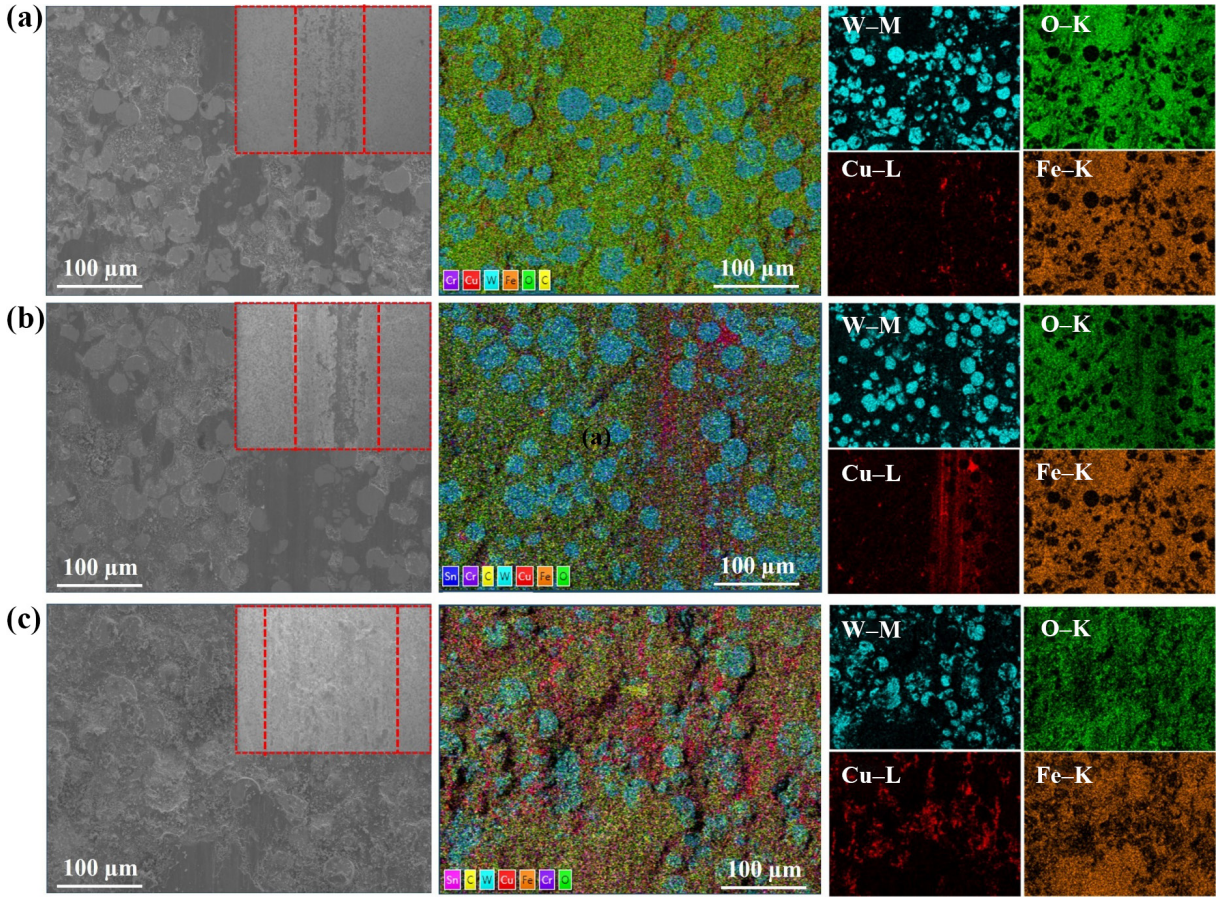

Fig. 7 SEM images and EDS mappings of wear track morphology of BJPWC after tests under different steel counterparts: (a) GCr15 ball, (b) HSS ball, and (c) 304 ball.

Among all counterpart balls, SiC exhibits the highest thermal conductivity (120 W/(m·K)), allowing frictional heat to dissipate rapidly. This reduces the formation of localized high-temperature zones and consequently lowers the oxidation rate at the sliding interface. The diameters of the wear scars on the balls are 1.13, 0.82, 0.96, 1.58, 1.07, and 2.44 mm for Si_3N_4, ZrO_2, SiC, GCr15, HSS, and 304 balls, respectively. The wear scar diameter of steel balls is much larger than that of ceramic balls, which is mainly related to the difference in hardness values between different balls. For example, the hardness of SiC and HSS is 27.4 and 2.1 GPa, respectively. The severe surface wear of steel balls is not only related to the low hardness and elastic modulus, but also to different wear mechanisms, which are the main factors affecting the amount of wear. Therefore, WC/bronze composite/SiC is the optimal combination in terms of the wear volume of the disc and wear loss of the counterpart.

The above results indicate that the most favorable tribological performance is obtained when sliding against SiC, which results from the nearly continuous tribofilm. To further explore the composition and structure of this tribofilm, FIB and STEM analyses were conducted. The FIB specimen contains both the smooth tribofilm region and the WC particle region, as can be seen in Fig. 9(a). As the WC and bronze have different strengths, the soft bronze is more easily milled than the WC; thus the prepared FIB seems not to be perfect. STEM results in Fig. 10(b) indicate that the tribofilm is mainly oxide. It is about 3 μm in thickness, which is rich in Si, O, C, Cu, Sn, and W.

The bright field (BF) image and the corresponding EDS mappings of the oxide region in Fig. 9(c) are illustrated in Fig. 10. At the tribofilm, the strong oxygen signals indicate that the tribolayer contains mainly oxide, from oxidized wear debris of bronze and WC from the plate, and SiC from the counterpart ball, which are identified by the aggregation of W, Si, and Cu at some regions. It is hard to exactly identify the phase of the oxide, which contains Cu, O, Si, W, Sn, and minor C. The line scan in Fig. 10(c) shows the normalized elemental counts, indicating high concentrations of Cu, O, Si, and W in the tribofilm. This phase is designated as the O–Cu–W–C composite. Apart from a few micrometer-scale WC and bronze debris, most of the worn material is nanoscale and enclosed within the white region, which likely corresponds to the amorphous phase. It can be assumed that during sliding, the generated wear debris undergoes fragmentation, compaction, oxidation, and sintering, resulting in the formation of nanoscale debris.

To further explore the microstructure of the tribofilm, high-resolution transmission electron microscopy (HRTEM) analysis was conducted at the red box-marked region in Fig. 10(a). The atom-resolved HRTEM image presents some crystalline regions surrounded by an amorphous phase. The fast Fourier transform (FFT) patterns on regions marked with different colors in HRTEM images (Figs. 11(a2) and 11(b2)) can further confirm the amorphous–crystalline structure of the tribofilm. The crystals embedded in the amorphous matrix are either bronze from the substrate or WC particles from the counterpart ball. The crystal structure in the friction film is mainly composed of Cu and WC crystals in the original WC/bronze composite, surrounded by an amorphous matrix of silicate glass (Cu/W–Si–O).

4 Discussion

The dependence of the tribological performance of the BJPWC sliding against different counterparts was studied. The results

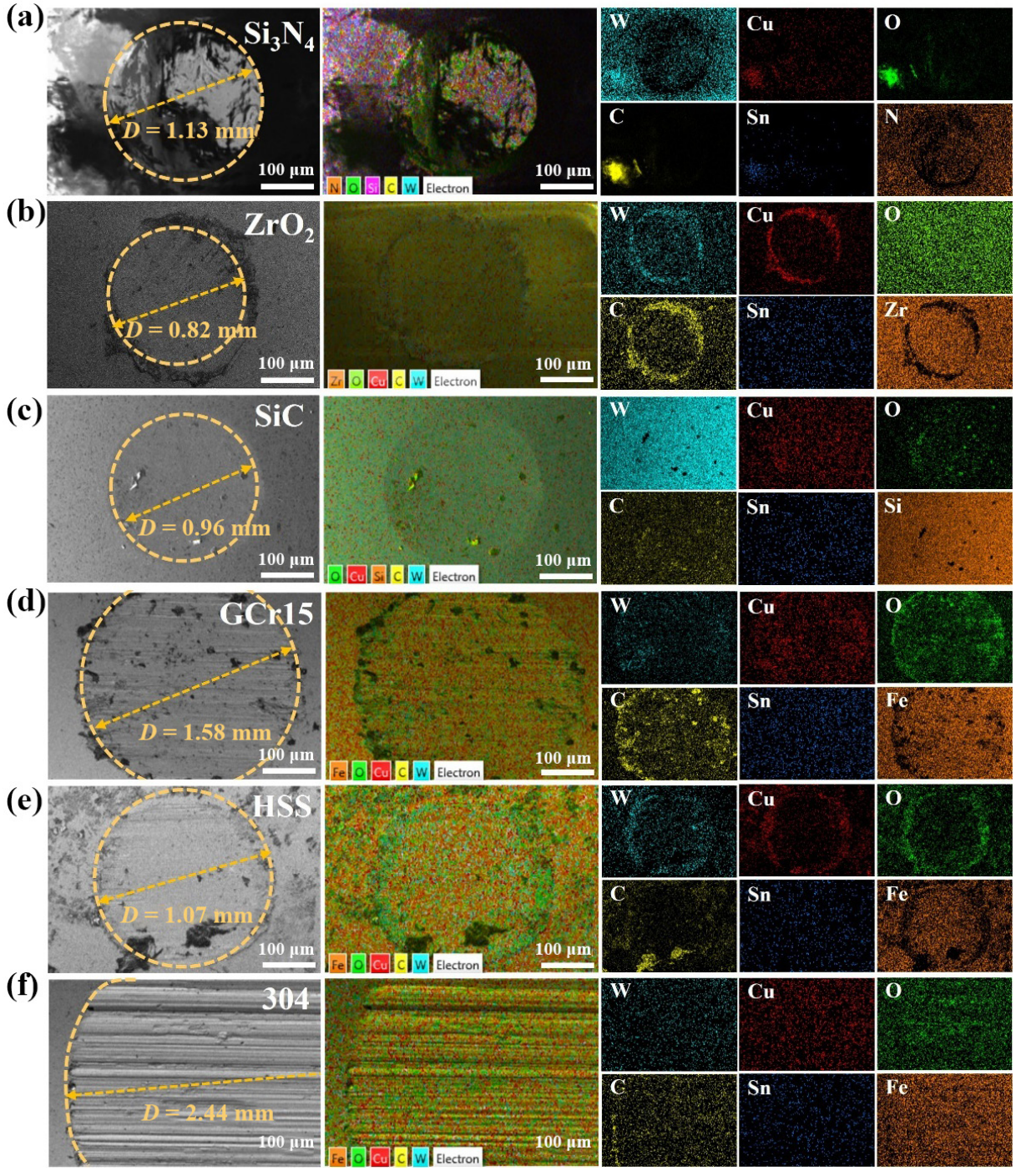

Fig. 8 SEM images and corresponding EDS mappings of wear scars of different counterpart balls after friction test of load from 5 to 80 N: (a) Si_3N_4 ball, (b) ZrO_2 ball, (c) SiC ball, (d) GCr15 ball, (e) HSS ball, and (f) 304 steel ball.

suggest that the frictional results are heavily counterpart-dependent. For the ceramic balls, the COF curves are more stable, with the wear volume of the counterparts lower than that of the steel balls. This difference is not only related to thermal conductivity, hardness, and modulus, but also to the chemical composition of the counterpart materials, leading to differences in tribofilm forming ability.

4.1 Influence of mechanical properties on tribological performance

In Archard's theory, $W = k(P/H)$, where W is the wear rate, k is the pre-factor relative to the ductility of the material, and P and H are the applied load and hardness, respectively [32]. However, for the BJPWC plate sliding against different balls, its wear seems inversely related to the hardness of the counterpart ball, where the hardest SiC ball leads to the lowest wear of the BJPWC. This is contrary to the imaging that the hardest ball will cause the heaviest devastation of the plate. Generally, the anti-wear performance of the counterpart is proportional to its hardness, especially when comparing the ceramic balls (ZrO_2 and SiC) with the steel balls (HSS and 304). However, this is not exactly the case when comparing the results under different ceramic balls. The SiC is the hardest among all the counterparts and its wear (diameter of the wear scar is 0.96 mm) is higher than ZrO_2 (diameter of the wear scar is 0.82 mm), although both are lower than those of other

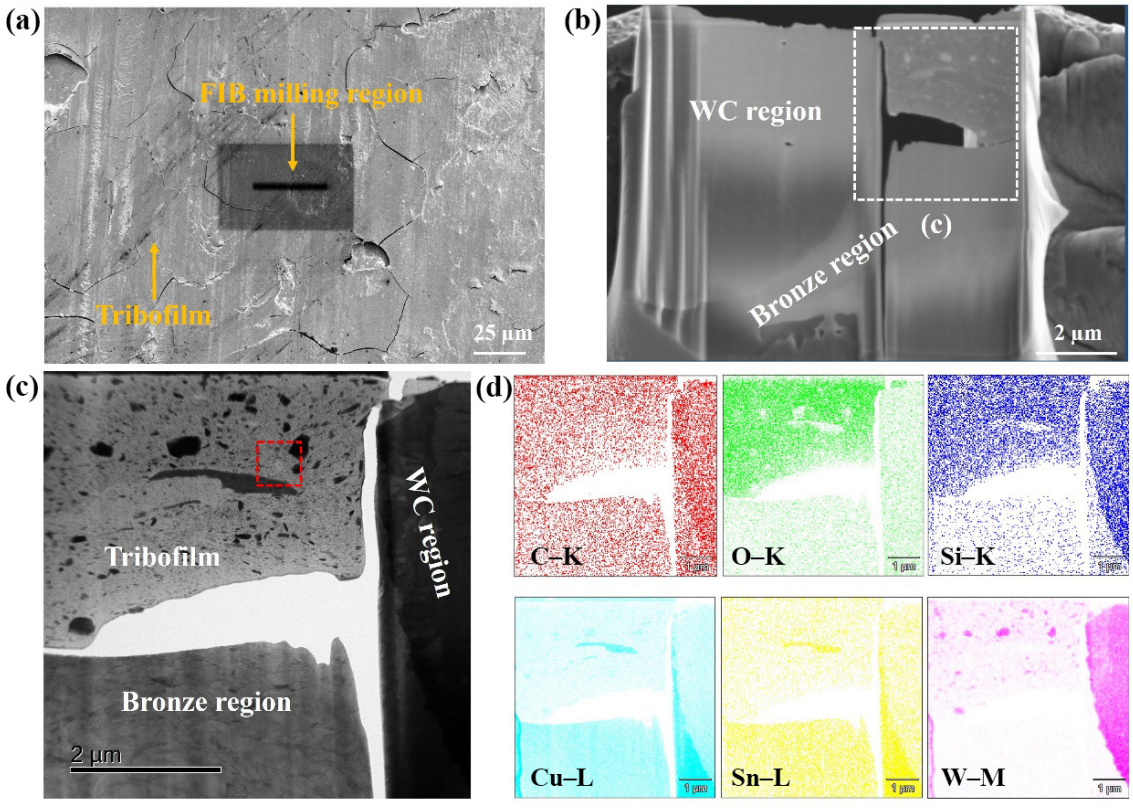

Fig. 9 FIB and STEM observation of worn surface of BJPWC after sliding against SiC: (a) FIB milling region, (b) cross-section of worn interface, (c) high-angle annular dark-field (HAADF) image of marked white box region in (b), and (d) corresponding EDS elemental mappings of (c).

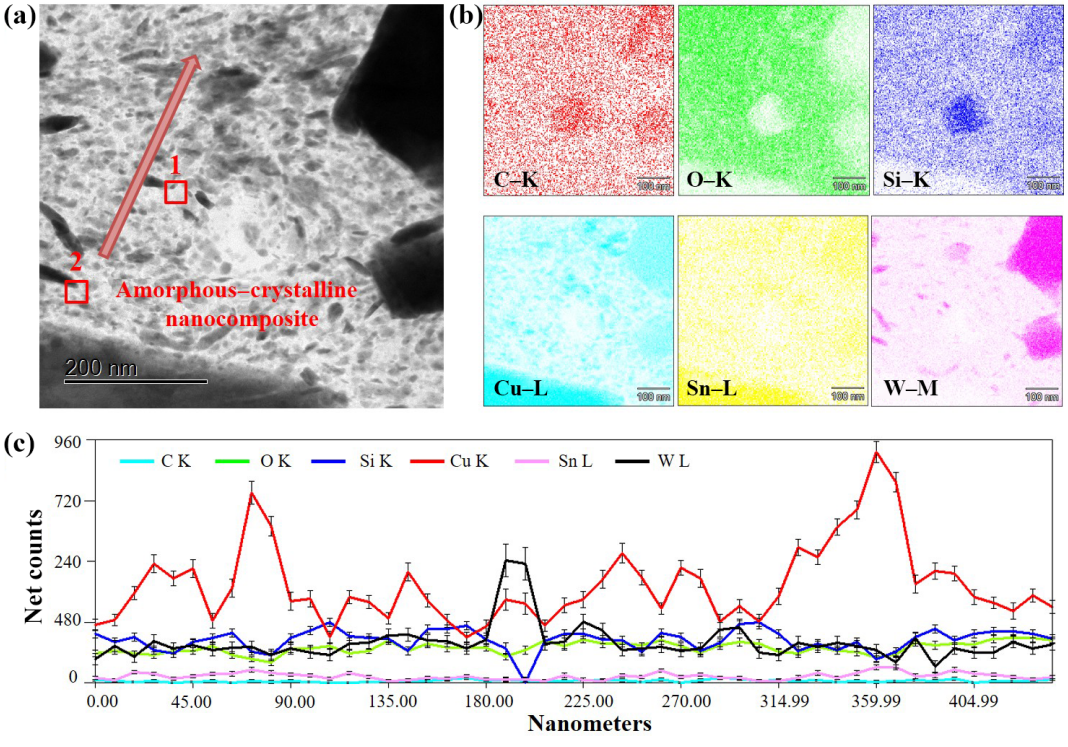

Fig. 10 (a) BF image of the region marked by the red box in Fig. 9(c). (b) EDS mappings of (a). (c) Line scan of red arrow in (a).

counterparts (Fig. 8). This result can also be identified for the Si_3N_4, where the slightly higher hardness of Si_3N_4 is correlated to lower wear of the BJPWC plate but higher wear of the ball. For the steel balls, HSS and GCr15 balls with higher hardness than 304 show better wear resistance. The heavy wear for 304 steel balls results from the weak abrasive resistance and poor capability in promoting the formation of a tribofilm at the sliding interface.

Thermal conductivity can also make a difference. Heat from continuous sliding can not only result in the oxidation of the worn interface, but also be the source of thermal fatigue, which will lead

to the development of cracks, spalling, and wear. It is believed that the best tribological performance of the BJPWC/SiC counterpart is also related to the excellent thermal conductivity of the SiC ball. The highest thermal conductivity of SiC among all the counterparts will transfer the heat rapidly from the interface and reduce the heat spikes, improving the thermal dissipation and redistributing thermal loading from dry sliding, which prevents the deterioration of the contact interface and the underlying matrix materials [33]. Therefore, the wear of the BJPWC under different ceramic counterparts is disproportional to the order of thermal conductivity. Some spalling regions exist on the BJPWC surface against ZrO_2, while the worn surface of BJPWC is generally smooth. SiC and Si_3N_4 showed negligible spalling. This can be attributed to the differences in thermal conductivity. The low thermal conductivity of ZrO_2 will lead to the aggregation of heat at the sliding interface, resulting in fatigue and spalling wear of the BJPWC, especially at the interface of WC particles and bronze.

To further elucidate the relationship between mechanical properties and wear behavior, a semi-quantitative comparison was conducted based on the hardness of the counterpart materials. The hardness of the counterparts follows the order: SiC > Si_3N_4 > ZrO_2 > HSS > 304, which generally corresponds to the observed trend in wear resistance. Counterparts with higher hardness tend to reduce the wear of the BJPWC plate, as evidenced by the lower wear when sliding against SiC and Si_3N_4 compared to steel counterparts. However, this relationship is not solely governed by hardness. For instance, despite the higher hardness of SiC compared to ZrO_2, the wear behavior also depends strongly on thermal conductivity and the stability of the tribological interface. Therefore, the wear performance is governed by a synergistic effect of mechanical and thermal properties rather than a single parameter.

The tribological behavior of the WC/bronze composite is closely related to the mechanical and thermal properties of the counterparts. SiC exhibits the lowest COF and wear volume, which can be attributed to its high hardness (27.4 GPa), high elastic modulus (440 GPa), and high thermal conductivity (120 W/(m·K)), enabling it to resist deformation and dissipate frictional heat effectively. In contrast, metallic counterparts such as GCr15, HSS, and 304 have lower hardness, leading to stronger adhesive wear and higher wear volumes, particularly for 304. Meanwhile, the low thermal conductivity of ZrO_2 (2 W/(m·K)) may cause heat accumulation at the interface, resulting in relatively higher friction and wear.

4.2 Influence of chemical composition on tribological performance

The tribological performance of the BJPWC sliding against different counterparts is also related to the chemical composition differences of the balls. Figure 12 shows the Raman spectra of WC/bronze composites after sliding against different counterparts. The characteristic D (~1,342 cm^{-1}) and G (~1,592 cm^{-1}) bands confirm the presence of disordered and graphitized carbon, while the 2D peak (~2,685 cm^{-1}) suggests a certain degree of structural ordering in the carbon layer. Moreover, the peak near ~666 cm^{-1}, especially observed for 304 steel counterparts, is attributed to iron oxides, indicating the occurrence of tribo-oxidation and material transfer from the counterpart. These results demonstrate that the friction process leads to the formation of carbonaceous and oxide films, which together play a key role in governing the tribological performance of the WC/bronze composite.

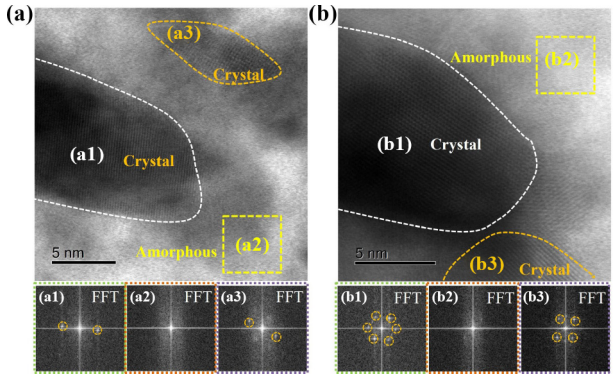

Fig. 11 HRTEM images of different typical regions in nanocomposite oxide layer and FFT results in Fig. 10(a). (a) Region 1 and (b) Region 2 of crystalline–amorphous nanocomposite layer.

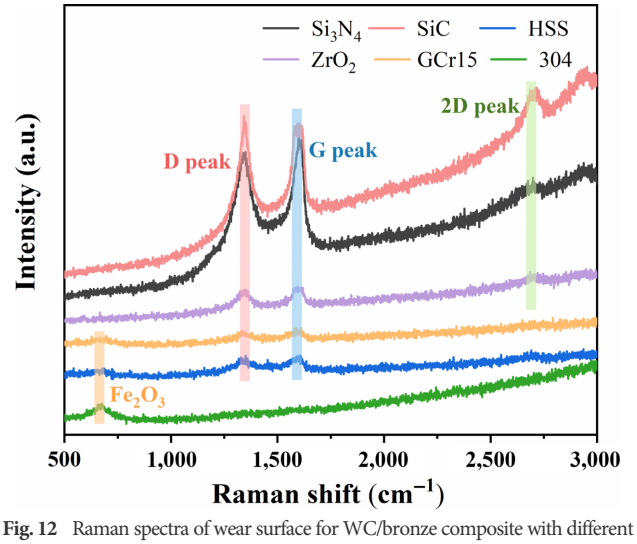

Fig. 12 Raman spectra of wear surface for WC/bronze composite with different counterpart balls.

The lowest wear rate, even negative wear volume, for the BJPWC plate against SiC and Si_3N_4 balls indicates that a protective tribofilm develops on the surface, consistent with the D, G, and 2D peaks. Si-containing ceramics exhibit higher wear resistance than ZrO_2, and the Si element facilitates the *in situ* formation of carbonaceous and oxide tribofilms at the interface. Compared with Si_3N_4, SiC balls with relatively high hardness and thermal conductivity are more beneficial to the formation of the tribofilm, as identified by the nearly continuous coverage of oxygen on the wear surface for SiC (Fig. 6(c)) and weaker coverage of O for Si_3N_4. The *in situ* formed continuous tribofilm can provide a low shear strength, which helps stabilize the COF and protect the BJPWC surface. The tribofilm consists of crystalline oxides embedded in an amorphous matrix. The oxide grains hinder crack propagation and dislocation motion, enhancing hardness, while frictional heat induces tribochemical reactions with ambient oxygen, forming a lubricious coating [34]. Si can lead to the *in situ* formation of the amorphous phase for effective lubrication. It was also reported by other researchers that Si-containing ceramic balls can lead to the formation of silicate glass that can reduce friction and wear [35].

4.3 Crystal–amorphous nanocomposite layer improves friction performance

Previous studies have shown that amorphous–crystalline nanocomposites, in which nanocrystals are embedded within an

amorphous matrix, exhibit a remarkable combination of high strength and excellent ductility, arising from the compatible flow behavior between the amorphous and crystalline phases [36]. The mechanical behavior of the amorphous–nanocrystalline composite structure can be understood based on the synergistic effects between the amorphous matrix and the embedded nanocrystalline domains. The amorphous phase inherently exhibits limited deformability due to the mechanical instability of the major shear bands [37, 38]. Under cyclic loading, local stress concentration can trigger brittle cracking, which in turn promotes micro-cutting and accelerates wear [39]. However, the abundant interfaces between the amorphous matrix and nanocrystalline grains are critical to regulating the deformation behavior. These interfaces can promote mechanisms such as interface sliding and crack deflection, which hinder crack propagation and improve the fracture resistance of the tribofilm [2, 35]. Furthermore, the heterogeneous structure can distribute the applied stress more uniformly and suppress localized stress concentration [40, 41]. As a result, the amorphous–nanocrystalline composite structure enhances the structural stability of the friction film during sliding, thereby contributing to improved tribological performance. The Cu/W–Si–O amorphous matrix, with a disordered network and no slip planes, acts as a "buffer layer" that absorbs frictional stress and distributes load, preventing direct contact between hard WC and SiC phases. Embedded Cu and WC nanocrystals provide load-bearing support, maintaining mechanical strength and thermal stability. The crystal–amorphous interfaces, with high interfacial energy, promote local atomic relaxation, absorb energy during shear, and hinder crack propagation. Meanwhile, the crystalline–amorphous oxide layer accommodates most plastic deformation during friction, significantly enhancing wear resistance (Fig. 13).

At higher loads (5–80 N), Si/SiO_x is released during the friction process of SiC counterpart ball at room temperature, arising from the combined effects of strong local shear, contact pressure, and frictional chemical reaction [42]. These chemicals undergo intense chemical/structural coupling with WC/bronze (W, Cu, Sn, Zn, and interfacial oxygen). The crystal structure will be disrupted, and atomic diffusion will be limited. Negative mixing enthalpy and network chemical bonds (Si–O, W–Si, Cu–Si, etc.) make it difficult to reconstruct long-range order at high strain rates [43, 44]. Thus, a short-range ordered and long-range disordered amorphous tribofilm is formed and stabilized at the interface. Among them, Si atoms can serve as a chemically active center to provide network-forming ability, change interface bond types and mixing enthalpy, which is beneficial for the thermodynamic stability of amorphous phases [45, 46]. This dynamically promotes amorphous formation by inhibiting diffusion/recrystallization and promoting shear-induced structural collapse. The mixing enthalpy of Si atoms with other elements is shown in Table S2 in the ESM. The mixing enthalpy between Si and Si with O, W, Cu, etc. is usually negative, indicating that the formation of Si-containing network structures can significantly reduce the system's free energy. These heterogeneous chemical bonds have strong covalent properties and significant directionality, which can disrupt the long-range ordering of metal bonds. Therefore, the diffusion of Si makes the "Si-containing amorphous composite" thermodynamically more stable, reducing the driving force for returning from the amorphous to crystalline state.

5 Conclusions

This work compares the tribological performances of different counterparts (three types of ceramics and steels) sliding against BJPWC. The differences in the tribological results are responsible for the mechanical properties, thermal conductivity, as well as chemical composition of the counterparts. The BJPWC sliding against SiC exhibits stabilized COF curves, the lowest friction values, and excellent anti-wear performance, which can be attributed to the high hardness, high elastic modulus, and high thermal conductivity of SiC that help suppress deformation and dissipate frictional heat at the interface. The Si-containing SiC ball can deliver beneficial chemistry at the interface and contribute to the formation of a surface protective tribofilm. The tribofilm shows a crystal–amorphous structure, which promotes the formation of an easy-shearing interface and protection of the rubbing counterparts. It provides insights into the tribo-oxide formation mechanisms in friction and wear control, and the tribochemical reaction with the formation of a lubricious amorphous–crystal film. This study elucidates the difference in the tribological performance of different sliding counterparts and can provide insight into the selection of sliding counterparts for the potential usage of BJPWC.

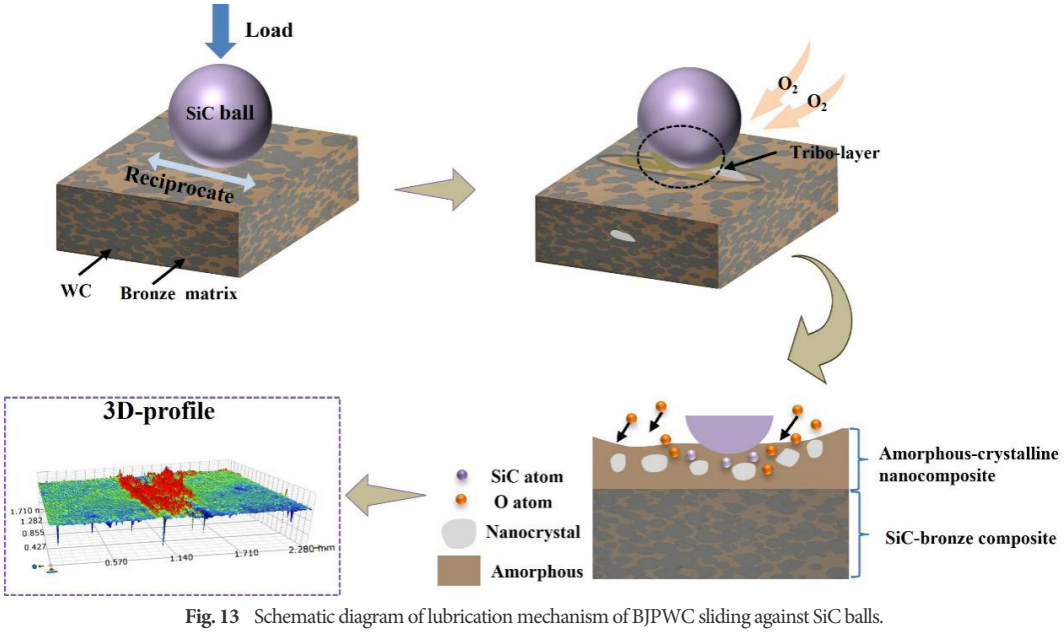

Fig. 13 Schematic diagram of lubrication mechanism of BJPWC sliding against SiC balls.

清華大学出版社 Tsinghua University Press | SciOpen

Acknowledgements

This work is supported by the National Natural Science Foundation of China (No. 52074231) and the Research Fund of the State Key Laboratory of Solidification Processing (NPU) (No. 2024-ZD-03) for the financial support of this work.

Author contributions

Xinyi Liu: Data curation, Validation, Writing manuscript, and Experimental design. Yi Ren: Software, Data curation. Xibo Shao: Software, Data curation. Jiangkun Fan: Conceptualization, Funding acquisition, Supervision, and Review and editing. Jinshan Li: Resources, Project administration.

Availability of data and materials

The data that support the findings of this study are available from the corresponding author upon reasonable request.

Competing interests

The authors have no competing interests to declare that are relevant to the content of this article.

Electronic Supplementary Material

Supplementary material is available in the online version of this article at https://doi.org/10.26599/FRICT.2026.9441271.

References

[1] Han J S, Wang S H, Ge W J, Chen H, Sun Y J, Ai Y X, Yuan W H, Ruan S Y, Niu W M, Yang H O, et al. Non-contact ultrasound to assist laser additive manufacturing. *Nat Commun* **16**: 7613 (2025)

[2] Seo J, Rao P, Raeymaekers B. Generating synthetic as-built additive manufacturing surface topography using progressive growing generative adversarial networks. *Friction* **12**(6): 1283–1298 (2024)

[3] He X, Li G, Zhang L, Huang Y H, Xie B Y, Shi Z F, Feng G H, Liu W B, Lyu F C, Wang S, et al. Bio-inspired material-structure-function integrated additive manufacturing of Al-based metamaterials with surpassing energy absorption. *Sci Adv* **11**(46): 0430 (2025)

[4] Chun S Y, Kim T, Ye B, Jeong B, Lee M J, Lee D H, Kim E S, Lee H, Kim H D. Capillary pressure and saturation of pore-controlled granules for powder bed binder jetting. *Appl Surf Sci* **515**: 145979 (2020)

[5] Hassanin H, Essa K, Elshaer A, Imbaby M, El-Mongy H H, El-Sayed T A. Micro-fabrication of ceramics: Additive manufacturing and conventional technologies. *J Adv Ceram* **10**(1): 422 (2021)

[6] Azhari A, Marzbanrad E, Yilman D, Toyserkani E, Pope M A. Binder-jet powder-bed additive manufacturing (3D printing) of thick graphene-based electrodes. *Carbon* **119**: 257–266 (2017)

[7] Cordero Z C, Siddel D H, Peter W H, Elliott A M. Strengthening of ferrous binder jet 3D printed components through bronze infiltration. *Addit Manuf* **15**: 87–92 (2017)

[8] Lu S L, Meenashisundaram G K, Wang P, Nai S M L, Wei J. The combined influence of elevated pre-sintering and subsequent bronze infiltration on the microstructures and mechanical properties of 420 stainless steel additively manufactured via binder jet printing. *Addit Manuf* **34**: 101266 (2020)

[9] Tripathy M, Gaskell K, Laureto J, Davami K, Beheshti A. Elevated temperature fretting wear study of additively manufactured Inconel 625 superalloy. *Addit Manuf* **67**: 103492 (2023)

[10] Chen L, Fu Z Q, Chen W P, Chen Z P, Xiong W, Zhu D Z, Lavernia E J. Enhancing mechanical properties and electrochemical behavior of equiatomic FeNiCoCr high-entropy alloy through sintering and hot isostatic pressing for binder jet 3D printing. *Addit Manuf* **81**: 103999 (2024)

[11] Bui H M, Großmann P F, Berger A, Seidel A, Tonigold M, Szesni N, Fischer R, Rieger B, Hinrichsen O. Comparison of Direct Ink Writing and Binder Jetting for additive manufacturing of Pt/Al_2O_3 catalysts for the dehydrogenation of perhydro-dibenzyltoluene. *Chem Eng J* **458**: 141361 (2023)

[12] Mudanyi R K, Cramer C L, Elliott A M, Unocic K A, Guo Q Y, Kumar D. W-ZrC composites prepared by reactive melt infiltration of Zr_2Cu alloy into binder jet 3D printed WC preforms. *Int J Refract Met H* **94**: 105411 (2021)

[13] Mostafaei A, De Vecchis P R, Kimes K A, Elhassid D, Chmielus M. Effect of binder saturation and drying time on microstructure and resulting properties of sinter-HIP binder-jet 3D-printed WC–Co composites. *Addit Manuf* **46**: 102128 (2021)

[14] Feng K H, Hu S D, Li L Y, Mao Y W, Heng Y H, Yuan J M, Wu J M, Wei Q S. Preparation of low residual silicon content Si-SiC ceramics by binder jetting additive manufacturing and liquid silicon infiltration. *J Eur Ceram Soc* **43**(13): 5446–5457 (2023)

[15] Cramer C L, Aguirre T G, Wieber N R, Lowden R A, Trofimov A A, Wang H, Yan J Q, Paranthaman M P, Elliott A M. Binder jet printed WC infiltrated with pre-made melt of WC and Co. *Int J Refract Met H* **87**: 105137 (2020)

[16] Do T, Kwon P, Shin C S. Process development toward full-density stainless steel parts with binder jetting printing. *Int J Mach Tool Manu* **121**: 50–60 (2017)

[17] Enrique P D, Mahmoodkhani Y, Marzbanrad E, Toyserkani E, Zhou N Y. *In situ* formation of metal matrix composites using binder jet additive manufacturing (3D printing). *Mater Lett* **232**: 179–182 (2018)

[18] Enrique P D, Marzbanrad E, Mahmoodkhani Y, Keshavarzkermani A, Al Momani H, Toyserkani E, Zhou N Y. Design of binder jet additive manufactured co-continuous ceramic-reinforced metal matrix composites. *J Mater Sci Technol* **49**: 81–90 (2020)

[19] Cui S G, Lu S L, Tieu K, Meenashisundaram G K, Wang L, Li X F, Wei J, Li W. Detailed assessments of tribological properties of binder jetting printed stainless steel and tungsten carbide infiltrated with bronze. *Wear* **477**: 203788 (2021)

[20] Wang L, Tieu A K, Lu S L, Jamali S, Hai G J, Zhu Q, Nguyen H H, Cui S G. Sliding wear behavior and electrochemical properties of binder jet additively manufactured 316SS/bronze composites in marine environment. *Tribol Int* **156**: 106810 (2021)

[21] Bouchafaa H, Maamache B, Boutaghou Z, Miroud D, Hebib M, Badji R, Cheniti B, Hvizdos P, Trujillo F J P, Alcalá G. Microstructure, mechanical performance, and wear behaviour of MMC (WC-W-Ni/Fe) obtained by infiltration. *Int J Refract Met H* **132**: 107291 (2025)

[22] Cheng R H, Luo X T, Huang G S, Li C J. Corrosion and wear resistant WC17Co–TC4 composite coatings with fully dense microstructure enabled by *in situ* forging of the large-sized WC17Co particles in cold spray. *J Mater Process Tech* **296**: 117231 (2021)

[23] Zhang Y Y, Choudhuri D, Scharf T W, Descartes S, Chromik R R. Tribologically induced nanolaminate in a cold-sprayed WC-reinforced Cu matrix composite: A key to high wear resistance. *Mater Design* **182**: 108009 (2019)

[24] Li Z Y, Yan H, Zhang P L, Guo J L, Yu Z S, Ringsberg J W. Improving surface resistance to wear and corrosion of nickel-aluminum bronze by laser-clad TaC/Co-based alloy composite coatings. *Surf Coat Tech* **405**: 126592 (2021)

[25] Zhang D Y, Peng Z J, Liu Z L, Yu J K, Yuan L. Study on wear protection performance of HVAF WC–Cr_3C_2–Ni coatings deposited on crystallizer surface. *Surf Coat Tech* **481**: 130640 (2024)

[26] Zhu Z X, Shi T Z, Chen W Y, Wang L J, Chen J J, Cheng J, Zhu S Y, Yang J. Effect of WC-17Co content on microstructure, mechanical properties, and tribological behavior of low-pressure cold sprayed tin bronze composite coating. *Surf Coat Tech* **465**: 129589 (2023)

[27] Jin K J, Qiao Z H, Zhu S Y, Cheng J, Yin B, Yang J. Friction and wear properties and mechanism of bronze–Cr–Ag composites under dry-sliding conditions. *Tribol Int* **96**: 132–140 (2016)

[28] Efremenko V G, Chabak Y G, Fedun V I, Shimizu K, Pastukhova T V, Petryshynets I, Zusin A M, Kudinova E V, Efremenko B V. Formation mechanism, microstructural features and dry-sliding behaviour of "Bronze/WC carbide" composite synthesised by atmospheric pulsed-plasma deposition. *Vacuum* **185**: 110031 (2021)

[29] Moskvichev E, Shamarin N, Savchenko N. High temperature tribological properties of additively manufactured WC reinforced CuAl7–W composites. *Wear* **556**: 205535 (2024)
[30] Luo J S, Sun W T, Liang D S, Chan K C, Yang X S, Ren F Z. Superior wear resistance in a TaMoNb compositionally complex alloy film via *in situ* formation of the amorphous–crystalline nanocomposite layer and gradient nanostructure. *Acta Mater* **243**: 118503 (2023)
[31] Hamdi H, Abedi H R, Zhang Y. A study on outstanding high-temperature wear resistance of high-entropy alloys. *Adv Eng Mater* **25**(12): 2201915 (2023)
[32] Telliskivi T. Simulation of wear in a rolling–sliding contact by a semi-Winkler model and the Archard's wear law. *Wear* **256**(7–8): 817–831 (2004)
[33] Voevodin A A, Muratore C, Aouadi S M. Hard coatings with high temperature adaptive lubrication and contact thermal management: Review. *Surf Coat Tech* **257**: 247–265 (2014)
[34] Strong K L, Zabinski J S. Thermal chemistry of a high temperature solid lubricant, cesium oxythiomolybdate Part II: Thermo-oxidative stability of Cs_2MoOS_3/Si_3N_4 mixtures. *J Mater Sci* **36**(22): 5415–5422 (2001)
[35] Liu C, Li Z M, Lu W J, Bao Y, Xia W Z, Wu X X, Zhao H, Gault B, Liu C L, Herbig M, et al. Reactive wear protection through strong and deformable oxide nanocomposite surfaces. *Nat Commun* **12**: 5518 (2021)
[36] Wu G, Balachandran S, Gault B, Xia W Z, Liu C, Rao Z Y, Wei Y, Liu S F, Lu J, Herbig M, et al. Crystal–glass high-entropy nanocomposites with near theoretical compressive strength and large deformability. *Adv Mater* **32**(34): 2002619 (2020)
[37] Wang J Y, Liu X J, Wu Y, Wang H, Ma D, Lu Z P. Clustering-mediated enhancement of glass-forming ability and plasticity in oxygen-minor-alloyed Zr–Cu metallic glasses. *Acta Mater* **261**: 119386 (2023)
[38] Inoue A, Zhang W, Zhang T, Kurosaka K. High-strength Cu-based bulk glassy alloys in Cu–Zr–Ti and Cu–Hf–Ti ternary systems. *Acta Mater* **49**(14): 2645–2652 (2001)
[39] Greer A L, Rutherford K L, Hutchings I M. Wear resistance of amorphous alloys and related materials. *Int Mater Rev* **47**(2): 87–112 (2002)
[40] Utsumi J, Ide K, Ichiyanagi Y. Cu/SiO_2 hybrid bonding obtained by surface-activated bonding method at room temperature using Si ultrathin films. *Micro Nano Eng* **2**: 1–6 (2019)
[41] Wu G, Liu S D, Wang Q, Rao J, Xia W Z, Yan Y Q, Eckert J, Liu C, Ma E, Shan Z W. Substantially enhanced homogeneous plastic flow in hierarchically nanodomained amorphous alloys. *Nat Commun* **14** (1): 3670 (2023)
[42] Reichenbach T, Moras G, Pastewka L, Moseler M. Solid-phase silicon homoepitaxy via shear-induced amorphization and recrystallization. *Phys Rev Lett* **127**(12): 126101 (2021)
[43] Idrissi H, Carrez P, Cordier P. On amorphization as a deformation mechanism under high stresses. *Curr Opin Solid St M* **26**(1): 100976 (2022)
[44] Yesudhas S, Levitas V I, Lin F, Pandey K K, Smith J S. Unusual plastic strain-induced phase transformation phenomena in silicon. *Nat Commun* **15**: 7054 (2024)
[45] Zhao S, Flanagan R, Hahn E N, Kad B, Remington B A, Wehrenberg C E, Cauble R, More K, Meyers M A. Shock-induced amorphization in silicon carbide. *Acta Mater* **158**: 206–213 (2018)
[46] Grützmacher P G, Rammacher S, Rathmann D, Motz C, Mücklich F, Suarez S. Interplay between microstructural evolution and tribo-chemistry during dry sliding of metals. *Friction* **7**(6): 637–650 (2019)

Xinyi Liu is a Ph.D. student in the School of Materials Science and Engineering at Northwestern Polytechnical University. His research mainly focuses on the mechanical properties and deformation mechanisms of β-titanium alloys, tribological behaviors, and wear resistance properties of metallic materials, including titanium alloys, high-entropy alloys, and additively manufactured alloys.

Jiangkun Fan is currently a professor and doctoral supervisor at Northwestern Polytechnical University. His current research interests mainly focus on advanced metal structural materials such as titanium alloys and superalloys, including phase transformation crystallography, strengthening and toughening mechanisms, and deformation micro mechanisms.

Jinshan Li is currently a professor and doctoral supervisor at Northwestern Polytechnical University, China. He is the director of the State Key Laboratory of Solidification Processing. His current research interests mainly focus on aerospace high-strength and tough titanium alloys, high-entropy alloys, amorphous alloys, and their composite materials.